A molecular dynamics-based analysis of the influence of strain-rate and temperature on the mechanical strength of PPTA crystallites

Brian MERCER[1,2], Edward ZYWICZ[2*] and Panayiotis PAPADOPOULOS[1,†]

[1]*Department of Mechanical Engineering, University of California, Berkeley, CA, USA*
[2]*Lawrence Livermore National Laboratory, Livermore, CA, USA*

Abstract

Molecular dynamic simulations are used to quantify how the mechanical behavior of PPTA crystallites, the fundamental building blocks of aramid fibers such as Kevlar®, depend on strain-rate, temperature, and crystallite size. The (axial) crystallite elastic modulus is found to be independent of strain-rate and decreases with increasing temperature. The crystallite failure strain increases with increasing strain rate and decreases with increasing temperature and crystallite size. These observations are consistent with crystallite failure being driven by stress-assisted thermal fluctuations of bonds within PPTA crystallites and the concepts of the kinetic theory of fracture. Appealing to reliability theory, a model is proposed that predicts the onset of both primary and secondary bond failure within a crystallite as of function of strain rate, temperature, and crystallite size. The model is parameterized using bond failure data from constant strain-rate molecular dynamic strain-to-failure simulations and is used to compute the activation volume, activation energy, and frequency for both primary and secondary bond ruptures.

Keywords: Kevlar®; aramid fibers; molecular dynamics; reactive potentials; rate-dependence; temperature-dependence; fracture.

---

*zywicz1@llnl.gov

†panos@berkeley.edu

1   Introduction

Synthetic polymer fibers play a key role in many engineering applications including fiber-reinforced composites, sporting equipment, and woven fabrics. Among the strongest of man-made polymer fibers are aromatic polyamides, or aramid fibers, with well-known examples being Kevlar® and Twaron®. Aramid fibers consist of long-chain molecules made from the monomer poly(p-phenylene terephthalamide) (PPTA), pictured in Figure 1. Northolt *et al.* [1] showed through X-ray diffraction that the microstructure of PPTA fibers can be defined by an orthogonal unit cell of single PPTA monomers with polymer chains parallel to the fiber axis. Over the years, a number of studies [2–7] have observed that PPTA fiber microstructure is comprised of crystallites between 60 and 600 nm in diameter made from PPTA chains of about 200 nm in length, with periodic defect planes consisting of collections of chain-ends located every 20–40 nm along the fiber axis. Additionally, the fibers exhibit a 0.1–1.0 nm thick outer skin where chain-ends are distributed randomly along the fiber axis, rather than organized into defect planes.

In our previous work [8], molecular dynamics (MD) simulations were conducted to study the dynamic tensile deformation response of PPTA crystallites containing different distributions of chain-end defects, but did not explore the strain-rate dependence of the crystallite response in detail. Yet, this is an important topic to address: aramid fibers used in projectile-resistant fabrics and armor are subjected to high rates of tensile loading, with strain-rates in the range of 1,000–10,000 s^{-1}. Hence, the dependence of the fiber constitutive response on the rate of loading merits spe-
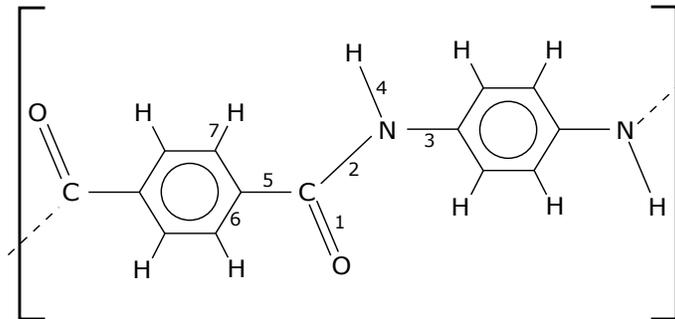

Figure 1: *Diagram of a single PPTA monomer. Unique bond types are labeled 1 through 7.*

cial attention. Dynamic tensile loading experiments performed on single yarns and fiber bundles have yielded conflicting results on this matter, with some experiments showing an increase in fiber modulus and tensile strength with increasing tensile strain rate [9–11], while others find no strain-rate sensitivity of the fiber mechanical properties [12–14]. Shim *et al.* [15] have postulated that the strain-rate sensitivity observed in their experiments is caused by differing fiber failure mechanisms, specifically failure by polymer chain scission along the backbone versus inter-chain sliding and hydrogen bond rupture between chains, which are activated at different rates; of course, this hypothesis cannot be easily verified experimentally. The lack of clarity on the existence and extent of rate-sensitivity in the mechanical properties of aramid fibers hinders the development of accurate constitutive models for fibers subjected to ballistic impact loading rates.

In this work, constant tensile strain-rate MD simulations are conducted on molecular models of PPTA crystallites in an effort to characterize their strain-rate dependent mechanical behavior. The crystallite is chosen as the subject of study due to its role as the fundamental building block of PPTA fibers and its length-scale compatibility with the limitations of MD modeling with respect to system size. Two interatomic potentials are employed to model PPTA: the reactive bond-order force field ReaxFF [16–19] is used to study situations where crystallite failure occurs by both primary and secondary (hydrogen) bond failure, while the classical PCFF force field [20] is used when failure occurs via hydrogen bond rupture only (the latter situation occurs when chain-end defects are clustered closely together, see [8]). The influence of temperature and crystallite size is also studied here in order to provide a more complete picture of the constitutive response of the crystallites. The results of these simulations show that the crystallite modulus decreases with increasing temperature but is unaffected by strain-rate and crystallite size, while crystallite strength depends prominently on strain-rate, temperature, and crystallite size. The findings on strength indicate that failure of PPTA crystallites is governed by thermal fluctuations of atomic bonds, which is consistent with the kinetic theory of fracture for failure in solids [21–23]. Leveraging this observation, a model for bond failure based on reliability theory is proposed, and it is shown that the onset of both primary and secondary bond failure in PPTA crystallites can be predicted with good accuracy over a range of strain-rates and temperatures.

The remainder of this article is organized as follows: Section 2 presents the details of the MD simulation methodology used here, including creation of the atomistic model of PPTA crystallites, interatomic force field selection, and the implementation. Section 3 presents the results of simulations concerning the sensitivity of the crystallite mechanical response to strain-rate, temperature, and unit cell size. In Section 4, a model for predicting bond failure based on the principles of reliability theory is presented and its predictive capacity is assessed. Concluding remarks and a discussion of the application of these results to creating a rate-dependent constitutive model of PPTA fibers are offered in Section 5.

2 Methods

2.1 Force field selection

The primary potential used in the simulations performed in this work is the ReaxFF force field [16–19]. ReaxFF is a reactive bond-order force field capable of dynamically modeling the breakage and formation of covalent bonds during a simulation. ReaxFF has been used extensively to study fracture events in atomistic solids [24–29], as well as specifically for PPTA [8, 30, 31], making it a good candidate for studying bond rupture events and the failure behavior of crystalline PPTA. While no ReaxFF parameter set has been specifically developed to model PPTA, our previous work [8] demonstrated that the parameter set developed by Liu *et al.* [32] is able to represent the behavior of PPTA reasonably well, and as such, this parameter set is again adopted for the simulations conducted here.

ReaxFF is a complex and computationally expensive force field, and its use is only necessary when performing simulations in which covalent bonds are expected to rupture. Therefore, for some of the simulations performed in this work, the more computationally efficient PCFF force field is used instead. PCFF is a Class-II force field [20] parameterized from *ab initio* calculations, and is designed specifically to model polymers and organic compounds. PCFF has been successfully used in several MD studies of PPTA [33–36], as well as in our previous work [8]. More recently, the COMPASS force field [37] (based on PCFF but modified to more accurately reproduce PVT relations in condensed matter) was employed by Grujicic *et al.* [38–
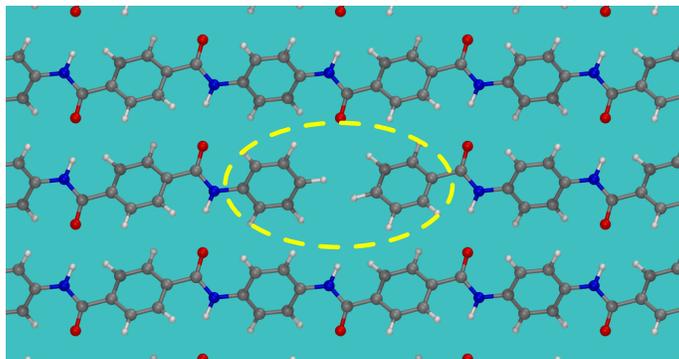
Figure 2: *A chain-end defect is introduced by removing the bonds linking two aromatic rings, and capping the rings with hydrogen atoms. The colors gray, blue, red, and white represent C, N, O, and H atoms, respectively.*

43] to conduct a variety of MD simulations of PPTA, exploring, among others, the effects of various classifications of defects and the effect of different static loading conditions on the material response. Given that PCFF was parameterized to model organic compounds like PPTA, and that it has been successfully used (along with its similar counterpart COMPASS) to model PPTA in previous MD studies, it is deemed a reasonable choice for modeling PPTA in cases where hydrogen (as opposed to covalent) bond rupture is of exclusive interest.

2.2 Molecular model

All the simulations performed in this work were conducted using LAMMPS [44], a parallelized MD code capable of handling large-scale atomic simulations. Initial atomic models of crystalline PPTA were created with the aid of Materials Studio [45]. Perfect crystal models were created from an atomic topology file based on the X-ray diffraction measurements by Northolt [1]. A perfect crystal model of any size can be created from this starting point by replicating the crystalline unit cell N_x, N_y, and N_z times in the x, y, and z directions, respectively. Some simulations in this work involve simulations of a crystallite containing chain-end defects. Chain-end defects are introduced by removing the amide linkage between two aromatic rings along the chain backbone and capping the aromatic rings with hydrogen atoms, as shown in Figure 2.

The MD simulations make use of periodic boundary conditions to represent PPTA

crystallites in a bulk environment. Hence, these simulations are most representative of the crystallites in the core of a PPTA fiber. In the case of a defect-free crystallite model, the PPTA chains are of effectively infinite length, since backbone chain bonds are continuous across periodic boundaries in the z-direction. Therefore, introducing chain-end defects into a crystallite model gives rise to a system consisting of finite-length chains. One model that is frequently used in this work consists of a simulation cell of $N_x \times N_y \times N_z$ crystalline unit cells, with one chain-end defect introduced into each chain. This yields a model in which each polymer chain is approximately N_z monomers in length. Thus, by changing the length of the simulation cell N_z and introducing defects at different locations, it is possible to easily create crystallite models of different polymer chain lengths and defect distribution patterns.

Two fundamental types of MD simulations are performed in this work. The first is the simulation of a PPTA crystallite under constant temperature and stress conditions, with the goal of obtaining time-averaged properties of the crystallite at these fixed conditions. To regulate the temperature and stress in these simulations, a Nosé-Hoover chain thermostat [46–48] was employed. Thermostat/barostat time constants of 100 fs for temperature and 1000 fs for pressure were used for both ReaxFF and PCFF simulations. The second type of simulation is the constant strain-rate deformation of a PPTA crystallite along the fiber axis. To conduct these simulations, the PPTA crystallite is first equilibrated at a stress-free state in order to obtain the equilibrium crystallite dimensions L_{x_0}, L_{y_0}, and L_{z_0}. Then, one end of the simulation cell is held fixed, while the other is displaced at a constant velocity $v_0 = \dot{\epsilon}_{zz} L_{z_0}$, where $\dot{\epsilon}_{zz}$ is the applied strain-rate. In addition, a barostat is employed to maintain zero time-averaged pressure on the lateral sides of the cell. An analogous methodology is used by Hossain *et al.* [49] for the study of dynamic strain-rate loading in amorphous polyethylene, and leads to dynamic uniaxial stress loading of the simulation cell via constant axial strain-rate deformation.

The ReaxFF and PCFF force fields have fundamentally different algorithmic implementations, and as such require different sets of simulation-specific settings. The ReaxFF force field parameters are specified from the parameter file in the supplemental material in [32]. For ReaxFF, a time step of $\Delta t = 0.25$ fs is used to integrate the equations of motion. ReaxFF uses the QEq charge equilibration method [50, 51] to compute and update atomic charges during the simulation, which is necessary

to accommodate changes in covalent bonding topology. The tolerance for the QEq algorithm is set to 1.0×10^{-6} coulomb, and the cutoff distance used for charged interactions is set to 10.0 Å. The implementation of the ReaxFF algorithms in LAMMPS is described in [52].

The PCFF force field parameters are obtained from Materials Studio using the tool `msi2lmp` packaged with the LAMMPS software. The Lennard-Jones coefficients for interactions between atoms of type α and β are determined using a mixing rule as follows:

$$
\begin{aligned}
\epsilon_{\alpha\beta} &= \frac{2\sigma_\alpha^3 \sigma_\beta^3 \sqrt{\epsilon_\alpha \epsilon_\beta}}{\sigma_\alpha^6 + \sigma_\beta^6} \\
\sigma_{\alpha\beta} &= \left(\frac{\sigma_\alpha^6 + \sigma_\beta^6}{2} \right)^{1/6}
\end{aligned} ,
\tag{1}
$$

where ϵ_α and σ_α (resp. ϵ_β and σ_β) are the Lennard-Jones parameters for atom type α (resp. β). The Lennard-Jones cutoff is set to 10.0 Å. Charge interactions in PCFF are computed using the PPPM method [53], with a relative force error tolerance of 1.0×10^{-4} for the solver, and a long-range cutoff of 10.0 Å. A time step $\Delta t = 1.0$ fs is used to integrate the equations of motion of the system.

3 Constant strain-rate loading simulations of PPTA crystallites

In this section, results from simulations involving tensile deformations of PPTA crystallites at different strain rates are presented. All simulations use the ReaxFF force field to allow for the possibility of chain failure via rupture of covalent bonds along the polymer chain backbone. For each simulation, the mechanical response of the crystallite is characterized by plotting the axial stress-strain curve (that is, σ_{zz} versus ϵ_{zz}) for the system. In each curve, the instantaneous stress is calculated using the standard MD stress formula [54]

$$
\sigma_{ij}^{MD} = \frac{1}{V} \sum_{\alpha=1}^{N} \left[-m^\alpha v_i^\alpha v_j^\alpha + \sum_{\beta > \alpha}^{N} (r_i^\beta - r_i^\alpha) f_j^{\alpha\beta} \right] ,
\tag{2}
$$

where indices α and β refer to atoms and indices i and j refer to vector components, such that m^α is the mass of atom α, v_i^α is the i-th velocity component of atom α, r_i^α

is the i-th position component of atom α, $f_j^{\alpha\beta}$ is the j-th force component acting on atom α due to its interaction with atom β, V is the volume of the atomic system, and N is the number of particles in the system. The engineering strain is computed as $\epsilon_{zz} = \dfrac{L_z - L_{z_0}}{L_{z_0}}$, where L_z is the deformed length of the crystallite at a given instant along the z-axis, and L_{z_0} is the unstressed equilibrium length of the crystallite in the same direction.

To explore the strain-rate sensitivity of a perfect crystallite, 25 constant strain-rate tensile loading simulations are conducted on a simulation cell consisting of 4×4×8 PPTA unit cells under periodic boundary conditions. Each chain is therefore infinitely long in the z-direction. Five simulations are run with each of the strain rates 5.0×10^9 s^{-1}, 1.0×10^9 s^{-1}, 2.0×10^8 s^{-1}, 4.0×10^7 s^{-1}, and 8.0×10^6 s^{-1}, with different (equilibrated) starting conditions prescribed to each simulation in order to explore the stochastic nature of the failure response, as observed in our previous work [8]. Figure 3 displays the results, which yield several important observations. The stress-strain response before the onset of failure is identical for each strain-rate: the behavior is nearly linearly elastic before failure, and the modulus of the system is independent of the applied strain-rate. The failure strain, however, does depend on the strain-rate, with the apparent trend being that an increase in strain-rate leads to an increase in failure strain. Also noteworthy is that Type 2 bonds (as diagrammed in Figure 1) are the first to fail in each chain over all strain rates examined, confirming that the failure mode and weak-link bond in the PPTA chains is independent of the rate of loading.

At this point it is important to emphasize that these constant strain-rate simulations become prohibitively costly with decreasing strain-rate, due to the large number of MD time steps required to reach crystallite failure strains at slower rates. After performing simulations at several different strain rates, it became evident that the response of the crystal is history-independent and reversible up until the first primary bond fails, as the system does not undergo any irreversible changes (*e.g.*, inter-chain slippage) hitherto. Additionally, the only strain-rate dependent property of the crystallite is the failure strain. Due to this very specific behavior, it is possible to initiate a strain-rate simulation from an elastically pre-strained state and obtain the same system behavior as beginning from zero strain, as long as bonds do
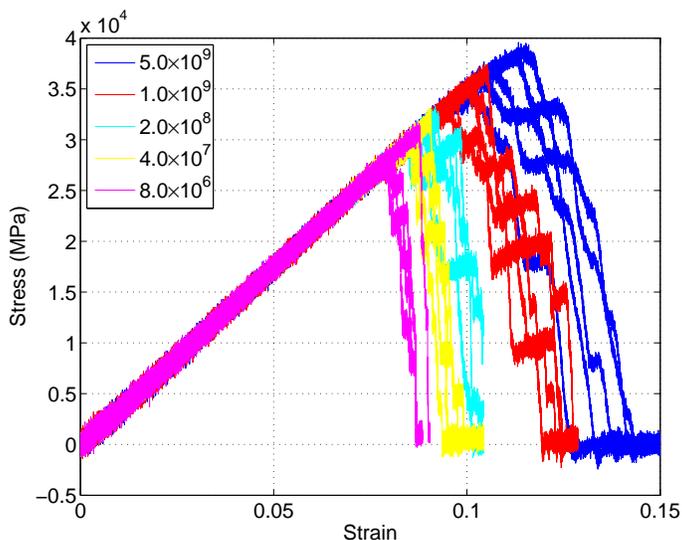
Figure 3: *Stress-strain curves for the 4×4×8 unit cell system at five different strain rates (in s^{-1} units) as indicated in the figure legend. Five different equilibrated starting points are used for each rate.*

not rupture at the starting strain during the process of loading at the desired rate. Exploiting this fact, strain-rate simulations at rates lower than 2.0×10^8 s^{-1} were performed by first pre-straining the system to a level of 7%, which was deemed a sufficiently low strain such that bond ruptures would never be observed for the strain-rates simulated in this work. The system was equilibrated at this starting point, and then the desired strain-rate was applied to simulate the constant strain-rate response. Using this method, it was possible to perform a single strain-to-failure simulation of a 4×4×8 unit cell system (7,168 atoms) at a strain-rate of 8.0×10^6 s^{-1} (the slowest rate simulated in this work) with about 160 hours of wall-clock simulation time (equivalently, about 10,000 CPU hours) using 64 processors. It should be noted that simulating strain-rates observed in typical engineering applications of aramid fibers, such as ballistic impact events where strain-rates are in the neighborhood of 100–1,000 s^{-1} [55], is, therefore, wholly impractical.

Another important aspect to consider is the influence of temperature on the crystallite stress-strain response. So far, all simulations have been performed at a constant temperature of 300 K. Figure 4 includes stress-strain curves of simulations performed at a strain-rate of 1.0×10^9 s^{-1} and temperatures of 300 K, 400 K, and
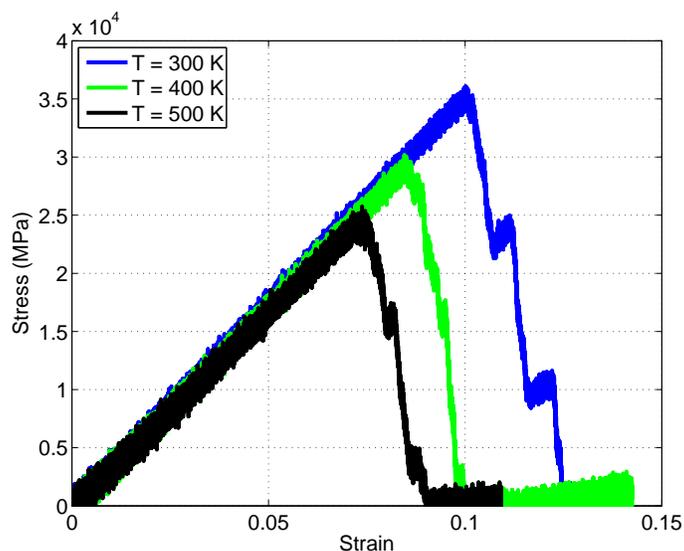
Figure 4: *Stress-strain curves for the 4×4×8 perfect crystal model at a strain-rate of $\dot{\epsilon}_{zz} = 1.0 \times 10^9 \ s^{-1}$ and temperatures of 300 K, 400 K, and 500 K.*

500 K for the 4×4×8 perfectly crystalline simulation cell. In each case, the stress response is nearly linearly elastic until failure, with the failure strain decreasing with increasing temperature. The modulus of the material also decreases with increasing temperature, taking (fitted) values of 320, 309, and 293 GPa (at strains below 1%) at temperatures of 300 K, 400 K, and 500 K, respectively.

To examine the full spectrum of temperature and strain-rate dependence of crystallite failure, the same set of strain-rate simulations as depicted in Figure 3 (with the exception of $\dot{\epsilon}_{zz} = 8.0 \times 10^6 \ s^{-1}$, due to its high computational cost) were performed at temperatures of 400 K and 500 K. Note that in these cases pre-straining in low strain-rate simulations was effected only to 3% (rather than the 7% used for 300 K) due to an anticipated lower failure strain at elevated temperature. Plots of failure strain versus strain-rate for all simulations performed at temperatures of 300 K, 400 K, and 500 K are displayed in Figure 5, which depicts a roughly linear relation between failure strain and log strain-rate for all temperatures examined.

In addition to strain-rate and temperature, it was observed that the size of the simulation cell also influenced the failure strain. To illustrate this point, a large system of 8×8×64 unit cells is subjected to tensile loading at strain-rates of $5.0 \times 10^9 \ s^{-1}$ and $1.0 \times 10^9 \ s^{-1}$ at a temperature of 300 K. The results are plotted in
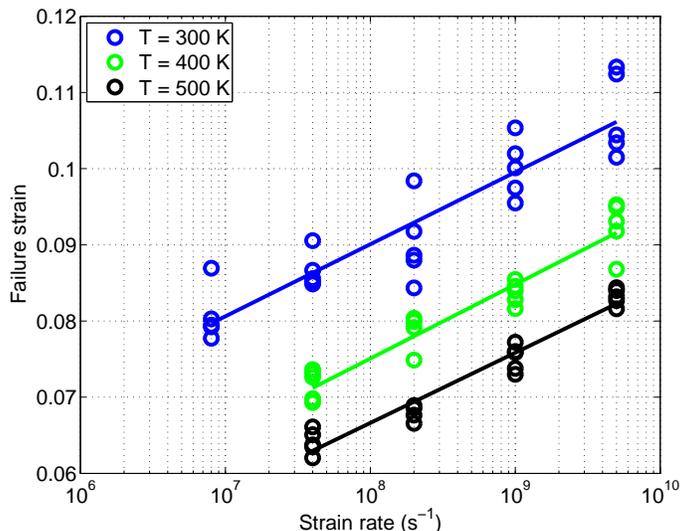
Figure 5: *Failure strain versus strain-rate for the 4×4×8 perfect crystal model at temperatures of 300 K, 400 K, and 500 K. The solid lines emphasize the apparent trend of a linear relationship between failure strain and log strain-rate over the rates and temperatures examined here.*

Figure 6 together with simulations at the same rate but using the 4×4×8 unit cell system. In each case, the larger system fails at a lower strain compared to the smaller system. This can be explained by recalling that the onset of failure is essentially due to an induced flaw in the material; in this case, the rupture of a primary bond in the system. In a larger crystal, there is a greater number of bonds that may fail, and as such, the larger system will, on average, fail sooner than a corresponding smaller system with fewer potential sites for failure. This behavior reflects the influence of size effects commonly observed in engineering materials, whereby larger material samples exhibit lower strength due to the increased likelihood of critical material defects in larger samples.

The simulations considered so far involve failure of a crystallite due to the failure of primary bonds along the polymer chain backbone. This is the only failure mechanism possible when considering chains of infinite length. Our previous work [8] concluded that failure via hydrogen bonds occurs only when chain-end defects are sufficiently clustered as to induce stress concentrations in nearby hydrogen bonds and facilitate inter-chain slippage. The weakened intermolecular bonds between polymer
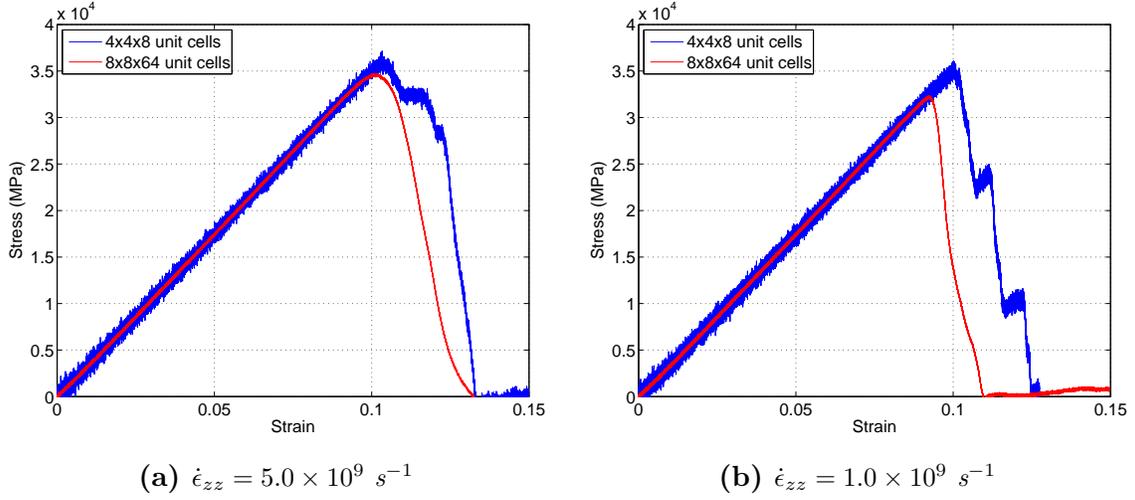
(a) $\dot{\epsilon}_{zz} = 5.0 \times 10^9 \ s^{-1}$

(b) $\dot{\epsilon}_{zz} = 1.0 \times 10^9 \ s^{-1}$

Figure 6: *Stress-strain curves for the 4×4×8 and 8×8×64 unit cell systems, highlighting the lower failure strain for larger systems.*

chains lead to chain slippage as the favored failure mechanism, as in the MD study of polyethylene (a crystalline polymer with relatively weak lateral bonding between chains) by O'Connor and Robbins [56], where chain sliding was found to be the favored failure mechanism. To determine whether failure dominated by hydrogen bond rupture exhibits the same trends with strain-rate and temperature as failure dominated by backbone chain bond rupture, a crystallite containing 4×4×8 unit cells with one chain-end defect per chain is considered. Due to the periodicity of the boundary conditions, this yields a crystallite model consisting of chains approximately 8 monomers in length with randomly distributed chain-end defect sites. Note that this is a relatively high concentration of defects compared to true PPTA, but mimics the clustered defect planes experimentally observed in [5] without incurring the high computational cost of simulating the system at true size. Preliminary strain-to-failure simulations with this crystallite showed that only the chain-sliding failure mechanism occurs, and primary bonds never rupture, as desired.

Using this simulation cell, five strain-to-failure simulations are conducted at 300 K at each of the strain-rates $5.0 \times 10^9 \ s^{-1}$, $1.0 \times 10^9 \ s^{-1}$, $2.0 \times 10^8 \ s^{-1}$, and $4.0 \times 10^7 \ s^{-1}$ (a total of 20 simulations). In order to explore the temperature-dependent response, five strain-to-failure simulations are conducted at a strain rate of $1.0 \times 10^9 \ s^{-1}$ for each of the temperatures 50 K, 100 K, 200 K, and 400 K (an additional 20
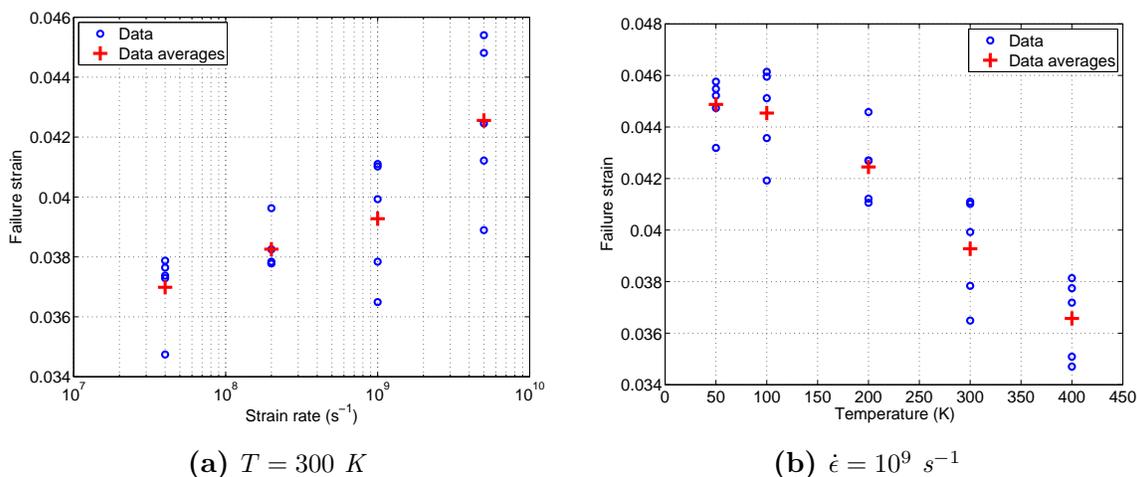
(a) $T = 300\ K$ **(b)** $\dot{\epsilon} = 10^9\ s^{-1}$

Figure 7: *Failure strain versus strain-rate for the 4×4×8 simulation cell with chains 8 monomers in length at (a) fixed temperature and (b) fixed strain-rate.*

simulations). The results are summarized in Figure 7, and show that the same trends observed in crystallite failure via primary bond rupture are present in crystallite failure via hydrogen bond rupture: that is, crystallite failure strain increases with increasing strain-rate and decreasing temperature.

4 A reliability theory-based model for prediction of bond failure

In this section, a model based on reliability theory is proposed for predicting the failure of both covalent and hydrogen bonds in crystalline PPTA. The model, parameterized by MD simulation results, demonstrates the kinetically driven nature of bond failure events in PPTA and also offers a way to make predictions about the onset of bond failure at lower strain rates than those accessible by MD simulation.

4.1 The kinetic theory of fracture and its parallels with reliability theory

The kinetic theory of fracture (KTOF) [21–23, 57] has been use to predict creep lifetimes of a wide array of metallic and polymeric solids. According to this theory, as bonds oscillate about their mean length at a given temperature, each oscillation represents an opportunity for the bond to rupture, and the probability of rupture

is determined by the temperature and loading conditions of the solid. In a material under constant temperature and stress, it has been shown that the mean time-to-failure t_f of individual bonds in the system is described by

$$t_f \;=\; t_0 \exp\left[\frac{U_0 - \gamma\sigma}{k_b T}\right]\;,\tag{3}$$

while the reciprocal of equation (3) gives the average rate of failure of the bonds as

$$\lambda \;=\; \omega_0 \exp\left[\frac{-U_0 + \gamma\sigma}{k_b T}\right]\;.\tag{4}$$

In equations (3) and (4), σ is the stress on the sample, T is the temperature, k_b is the Boltzmann constant, and t_0, U_0, and γ are material constants. These material constants are typically given physical interpretations as follows: t_0 (resp. ω) represents the period (resp. frequency) of oscillation of atomic bonds in the system, U_0 the activation energy required for fracture, and γ the activation volume.

Equation (4) also represents the classical stress-assisted rate equation commonly used in dislocation-based creep formulations, and in the absence of any stress, degenerates to the Arrhenius or Eyring equation found in statistical mechanics, transition state theory and other fields. It can be concluded from equation (4) that increasing the stress on the system lowers the effective activation energy, leading to a higher bond failure rate. Similarly, an increase in temperature results in an increase in the magnitude of the thermal fluctuations of atomic bonds, leading to an increase in the probability of a bond rupture occurring per oscillation and thus raising the bond failure rate. Note that these behaviors are consistent with the observed trends of crystallite failure in Section 3.

If bonds at fixed temperature and stress can be thought to fail at a constant rate as predicted by equation (4), then it is possible to draw parallels between bond failure behavior and principles in reliability theory. Reliability theory is used in engineering applications to model components or systems of components characterized by probability distributions for system lifetime and failure rate. In general, the theory can be applied to systems with time-dependent failure rate, which is realized, for example, in KTOF if a time-dependent stress rate $\sigma(t)$ is used in equation (4).

In what follows, bond failure in MD simulations of PPTA is analyzed in the context of reliability theory, and a model for predicting the onset of bond failure is

proposed. For a complete background on basic concepts and equations in reliability theory, the reader is referred to [58]. A brief summary of important equations and concepts relevant to this work are given in Appendix A.

4.2 Primary bond failure rate at constant strain and temperature conditions

In this section, attention is focused on the bond rupture process when the crystallite is held at a fixed strain over a long period of time. KTOF predicts that the rate of bond rupture in a solid at fixed stress and temperature is constant in time and given by equation (4). In a crystallite containing defects, local bond stress levels are highly dependent on the bond's proximity to a defect site, as discussed in our previous work [8]. But when a crystallite is defect-free, all bonds of a given type can be assumed to exhibit the same average rate of failure at a given crystallite stress and temperature. Furthermore, since in perfect crystallites there is a clear one-to-one relation between stress and strain (before bond failure occurs), the rate of bond failure can be assumed to be a function of crystallite strain ϵ_{zz} and temperature T. This assumption remains true up until the first-bond failure occurs, after which the introduction of a defect in the system due to the ruptured bond will cause bonds to change their individual rates of failure according to their proximity to the initial bond rupture site. A final assumption made here is that individual bonds behave independently of one another in terms of their thermal fluctuation characteristics, which is reasonable up until the moment that the first bond failure occurs in the crystallite.

Under the preceding assumptions, one may take an approach grounded in reliability theory and regard thermally fluctuating bonds in a PPTA crystal as a system of components which fail over time. Consider a system of N components which are identical to one another and behave independently of one another. These represent individual bonds within the crystallite. Suppose these components are all simultaneously put into operation at time $t = 0$ and that each component has a constant failure rate λ_0, to be determined. To this end, one would record the time-to-failure for each component τ_i, $i = 1, \ldots, N$, and then compute the mean time to first-bond

failure t_{f_0} as

$$t_{f_0} = \frac{1}{N} \sum_{i=1}^{N} \tau_i . \tag{5}$$

Subsequently, the individual bond failure rate λ_0 may be calculated as

$$\lambda_0 = \frac{1}{t_{f_0}} . \tag{6}$$

Using equation (6) to compute the average failure rate of bonds in a single PPTA crystallite would, however, be incorrect, since the occurrence of the first-bond rupture in the crystallite will influence the likelihood of failure (therefore, the failure rate) of the remaining bonds. An alternative method for calculating the individual bond failure rate can be used by treating a crystallite as a series system of N components (bonds). This series system can be considered to have failed the moment any of the N bonds in the system fails. By gathering data on the time to system failure (that is, time-to-first-bond failure) for K such systems (each of which represents an equilibrated crystallite at different initial conditions), the mean time-to-failure for a system of N bonds can be computed as

$$t_{f_N} = \frac{1}{K} \sum_{i=1}^{K} \tau_{f_i} , \tag{7}$$

where τ_{f_i} represents the time-to-first-bond failure in system i. The mean rate of failure for a system of N bonds is then

$$\lambda_N = \frac{1}{t_{f_N}} . \tag{8}$$

Equation (8) represents the failure rate of a system of N bonds, each with identical rates of failure λ_0. Appealing to equation (A.5), it is possible to relate the system failure rate λ_N to the individual bond failure rate λ_0 through

$$\lambda_N = N\lambda_0 . \tag{9}$$

Therefore, it is possible to measure the rate of individual bond failure in a crystallite at fixed strain and temperature by observing the times to first bond failure for a finite number of crystallites which differ only in (equilibrated) initial conditions, and then relate the computed system failure rate λ_N to the individual bond failure rate λ_0 through equation (9).

To examine to failure rate of bonds under fixed temperature and stress conditions, two sets of simulations are performed. The simulations track failure of Type 2 bonds, which is the mechanism of interest for studying system failure. The goal of these simulations is twofold. First, it is desired to confirm that the failure rate of bonds in the crystallite at fixed temperature and stress is indeed constant. If it is, then the distribution of times to first failure will follow the exponential distribution as implied by equation (A.1). Second, given that bond failure rate is indeed constant, equations (7–9) will be used to compute the individual bond failure rate for Type 2 bonds in the crystallite. The first set of simulations uses a simulation cell of $3\times4\times2$ crystalline units cells, while the second uses a simulation cell of $4\times4\times8$ crystalline unit cells. For each set of simulations, the ReaxFF force field is employed, and the simulation cells are brought to an axial strain of $\epsilon_{zz} = 0.095$ while an NPT thermostat maintains a temperature of $T = 300$ K and zero pressure on the lateral sides of the simulation cell, thereby creating fixed temperature and stress conditions. A relatively high level of strain is imposed to ensure covalent bond rupture occurs without prohibitively long simulation times. For each set of simulations, 400 crystallite variants are created by assigning slightly different equilibrated starting conditions to the simulation cell. Then, the distribution of times to first-bond failure for each crystallite $i = 1, \ldots, K = 400$ is recorded.

The results of the two sets of failure data gathered from the simulations are presented in Figure 8. The figure shows that the computed distributions of times to first failure closely resemble the exponential distribution, supporting the hypothesis that the bond failure rate in each system is constant in time. The quantitative results of the simulations are also summarized in Table 1. The data demonstrate that the single bond failure rates in each system are different from one another, and that this difference is not likely accounted for by the 95% confidence interval for the estimate of the failure rate in each system. This result is not in agreement with the assumption made at the outset of this investigation, which is that bonds behave independently of one another, since this assumption implies that the individual bond failure rates are independent of system size, or equivalently, that the system failure rate λ_N is related to the single bond failure rate λ_0 through equation (9). This discrepancy in computed single bond failure rates may be due to the relatively small size of the systems considered here, where individual bonds in a given chain may
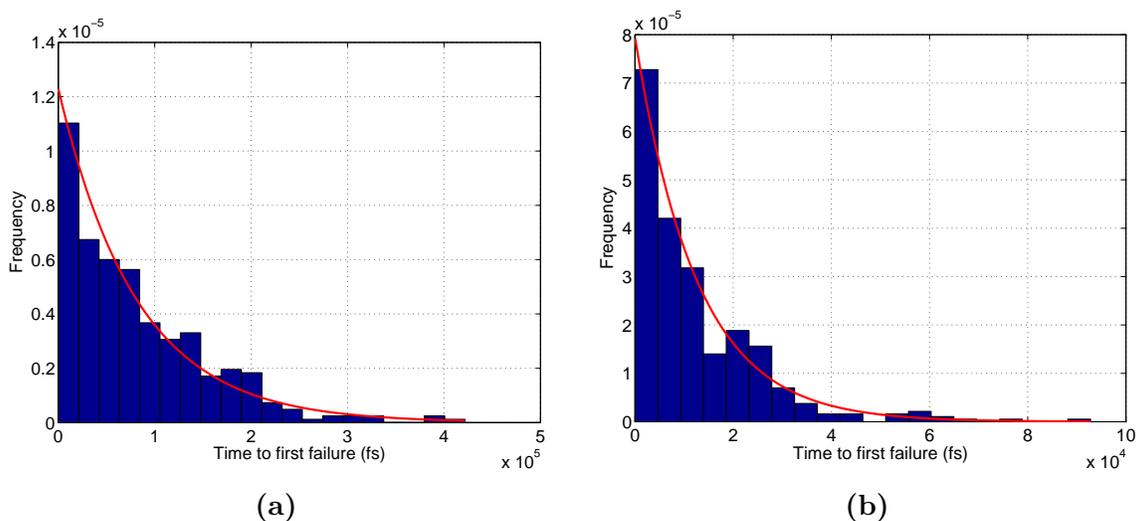
Figure 8: *The distribution of times to first failure for (a) the 3×4×2 system and (b) the 4×4×8 system. The red curves represent the exponential distribution with $\lambda_N = \frac{1}{t_{f_N}}$, where t_{f_N} is the average time-to-first-bond failure for the 400 simulations.*

not behave completely independently of one another. Consider, for example, that the overall length of the chain is fixed since the crystallite is at a fixed axial strain. Therefore, the sum of the bond lengths (projected onto the *z*-axis) along the chain is constrained to equal the length of the simulation cell, such that bonds may not take arbitrary lengths at any given moment in time. It is likely that if the times to first-bond failure were recorded for increasingly large systems, the value of λ_0 would eventually converge with increasing system size. However, due to the prohibitive cost of performing these simulations on such large systems, this investigation is not pursued here. Regardless of the accuracy of the calculation of the failure rate for a single bond in these perfectly crystalline systems, the exponential distributions displayed in Figure 8 indicate that the bond failure rate in a given crystallite is approximately constant at fixed strain and temperature.

It is also of interest to examine how the MD simulations predict a change in bond failure rate with a change in strain or temperature. To explore this, a set of simulations of the variety which produced the results displayed in Figure 8 is performed for a set of strains and temperatures of interest. Strain and temperature combinations are chosen to encourage bond failures to occur relatively quickly, otherwise, the sim-

Simulation cell size	N	t_{f_N} ($\times 10^{-15}$ s)	λ_0 ($\times 10^8$ s^{-1})	95% CI ($\times 10^8$ s^{-1})
3×4×2	96	$81,300 \pm 3720$	1.28	1.17–1.41
4×4×8	512	$12,600 \pm 661$	1.55	1.40–1.73

Table 1: *The failure rate of a single bond λ_0 is calculated based on the mean time to first failure t_{f_0} for the simulation data presented in Figure 8. The 95% confidence interval for the estimated value of λ_0 is shown in the final column.*

ulations take prohibitively long to run before the first-bond failure is observed. Each set of simulations at fixed strain and temperature generates a set of times to first failure, from which the individual bond failure rate is computed. Here, each set of simulations uses a system of 3×4×2 unit cells of perfectly crystalline PPTA and 200 variants on initial velocity conditions to generate the data points (with the exception of $\epsilon_{zz} = 0.095$ and $T = 300$ K, which has already been presented and uses 400 initial condition variants). Using more than 200 simulations per strain/temperature combination would increase the accuracy of the failure rate calculations, but is, again, prohibitively expensive.

The relations between failure rate and strain, as well as failure rate and temperature, are displayed in Figure 9. As anticipated, the bond failure rate depends strongly on both crystal strain and temperature. The curves displayed in Figure 9 are computed by finding the parameters from the KTOF equation (4) which best fit the data. Specifically, for the case of fixed temperature and varying strain, equation (4) predicts the following relation between bond failure rate and strain:

$$\lambda = A \exp\left[\alpha\epsilon\right] \ , \tag{10}$$

where $A = \omega_0 \exp\left[\dfrac{-U_0}{k_b T}\right]$ and $\alpha = \dfrac{\gamma E}{k_b T}$ are taken as constants. Here, it has been assumed that the relation between stress and strain is linearly elastic, so that $\sigma = E\epsilon$, which closely describes the stress-strain relation for PPTA crystals, as observed in Section 3. On the other hand, considering the case of fixed strain and varying temperature, equation (4) can be written as

$$\lambda = \omega_0 \exp\left[\frac{b}{T}\right] \ , \tag{11}$$

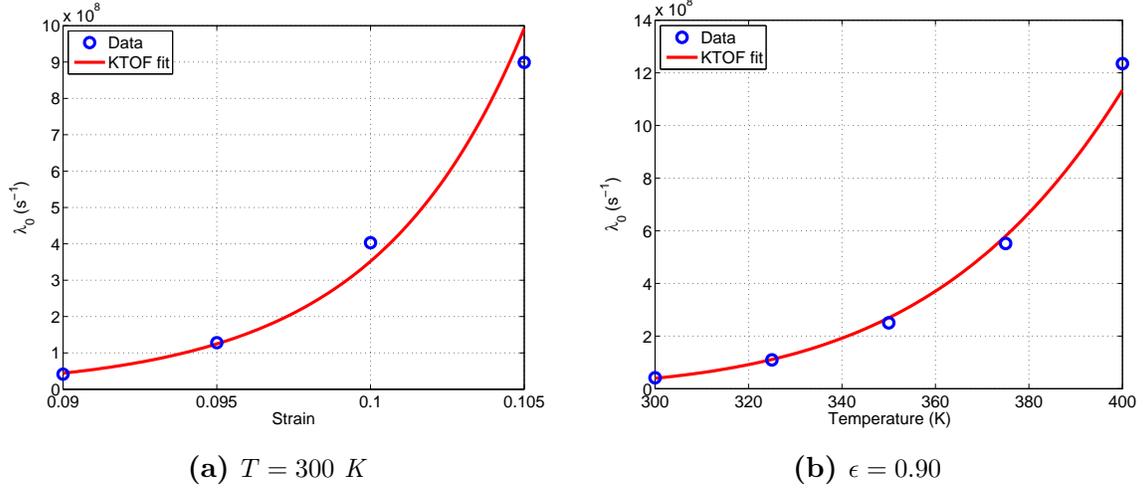**(a)** $T = 300\ K$ **(b)** $\epsilon = 0.90$

Figure 9: *Variation in primary bond failure rate with change in (a) strain and (b) temperature. Each data point (blue circles) represents failure rate data computed under fixed strain and temperature conditions. The red curve represents a fit of KTOF parameters to the data.*

where $b = \dfrac{-U_0 + \gamma E \epsilon}{k_b}$ and is assumed to be negative (as otherwise the strain would overcome the activation energy U_0 and bond rupture would immediately ensue). For negative b, an increase in temperature leads to a smaller negative exponent in equation (11), and the failure rate increases with increasing temperature.

From these curve fits, the parameters of equation (4) are calculated to be $U_0 = 80.6$ kJ/mol, $\gamma = 2.45$ Å^3, and $\omega_0 = 3.6 \times 10^{13}$ Hz. These values of the parameters are in line with typical ones observed in experimental data [23, 60]. The activation energy U_0 is somewhat low (covalent bond energies typically range from 100–300 kJ/mol), but the activation volume γ is of reasonable magnitude. In addition, the frequency ω_0 is close to the bond oscillation frequency of approximately 5×10^{13} Hz observed for Type 2 bonds in the MD simulations. These numbers are not meant to be interpreted as accurate estimates of the parameters in equation (4) in the sense that the measurements taken to obtain them are relatively few and somewhat inaccurate (due to the need for large numbers of simulations to get tight bounds on an estimate of the bond failure rate). However, the fact that equation (4) can be fit to the MD observations, and that this fit yields physically reasonable parameters for the activation energy, activation volume, and bond frequency is a

good indication that primary bond failure in these systems is well-described by the concepts embodied in the KTOF.

4.3   A model for primary bond failure under constant strain-rate loading

Concepts from KTOF and reliability theory are now applied to model bond failure under constant strain-rate loading. Exploiting the linear relation between axial stress and strain, the time-dependent stress is assumed to be $\sigma(t) = E\epsilon(t)$, where E is the Young's modulus of the crystallite and the subscript "zz" on E and ϵ is omitted for brevity. For generality, the temperature $T(t)$ is also assumed to be a function of time. Following equation (4), the failure rate of each bond may then be written explicitly as a function of time only as $\lambda_0(\epsilon(t), T(t)) = \lambda_0(t)$. Hence, bonds in a crystal subjected to time-dependent strain loading and temperature history can be thought of as having a time-dependent failure rate function $\lambda_0(t)$ and reliability theory concepts can be used to compute the mean time-to-failure, hence also mean strain-to-failure. The failure rate of a primary bond in crystalline PPTA is only easily predictable up to the moment of first-bond failure. After initial bond rupture, the conversion of bond potential energy into kinetic energy and the subsequent distortion of crystal structure near the bond rupture site make it difficult to predict how the failure rates of the rest of the bonds in the system will change. This means that the model may only reliably predict the onset of initial bond failure in a perfect crystal.

Consider the case of constant strain-rate loading $\epsilon(t) = \dot{\epsilon}t$ at a fixed temperature such that λ_0 is given by

$$\lambda_0(t, \dot{\epsilon}, T) = \omega_0 \exp\left[\frac{-U_0 + \gamma E \dot{\epsilon} t}{k_b T}\right] . \tag{12}$$

Appendix B details the derivation of the expression for strain at first-bond failure ϵ_{fb} using reliability theory, with the general expression given by equation (A.7). At high strain-rates, equation (A.10) gives an approximate expression for the strain at first bond failure – combined with equation (A.8), the expression

$$\epsilon_{fb} \approx \frac{k_b T}{\gamma E} \left[\ln \dot{\epsilon} + \ln\left(\frac{\gamma E}{\omega_0 N k_b T}\right) + \exp\left(\frac{U_0}{k_b T}\right) - G\right] \tag{13}$$

is obtained, where G is a constant. Note that equation (13) represents a linear relationship between strain at first-bond rupture and log strain-rate, which is consistent

with the trend postulated and shown in Figure 5 for crystallite failure strain versus strain-rate. Also noteworthy is that equation (13) is remarkably similar to that derived in [59] for failure stress in solids under constant stress-rate.

It is now desired to find the parameters U_0, γ, and ω_0 which best fit the strain at first-bond failure data generated from the simulations which produced Figure 5 (note that these strain values are different than the values plotted in Figure 5, which are for crystallite, rather than first bond, failure). To this end, an interior-point optimization algorithm (implemented with the KNITRO MATLAB software package [61]) is used to minimize an objective function which defines the error between the strain at first-bond failure data points and the model's predicted strain at first failure computed from equation (A.7). The objective function Φ is chosen as

$$\Phi(\mathbf{x}) \;=\; \sum_{i}^{N_{data}} \left[\epsilon_{fb_i} - \epsilon_{fb}(\dot{\epsilon}_i, T_i) \right]^2 \;, \tag{14}$$

where N_{data} is the number of observed first-bond failures (equivalently, the number of independent simulations performed), ϵ_{fb_i} is the ith observed strain at first failure and $\epsilon_{fb}(\dot{\epsilon}_i, T_i)$ is the expected strain first-bond failure computed using equation (A.7). The variable $\mathbf{x}$ is a vector of inputs, in this case the constants U_0, ω, and γ, to be fit to the data.

The results of the fit, along with the strain at first failure data points, are displayed in Figure 10. The deduced parameters provide a reasonably good fit to the data, especially when the error bars are taken into account. Note that the error bars are computed as the square root of the variance as given in equation (A.4); that is, the error bars emanate from reliability theory rather than KTOF or standard error in the data. The values of the parameters are $U_0 = 114$ kJ/mol, $\gamma = 4.40$ Å^3, and $\omega_0 = 4.0 \times 10^{13}$ Hz. These parameters are different than those obtained from fitting the data in Figure 9 to equation (4), but they are adequately close to one another, and, once again, represent physically reasonable values.

Plotted in Figure 11 is equation (A.7), using the above parameter values, for the three temperatures considered and a range of strain rates, some smaller than those simulated here. While not immediately apparent from equation (A.7), the failure strain for a fixed temperature tends toward zero as the strain rate goes toward zero. In addition, the time to first-bond failure is increasing rapidly. Hence, even at very
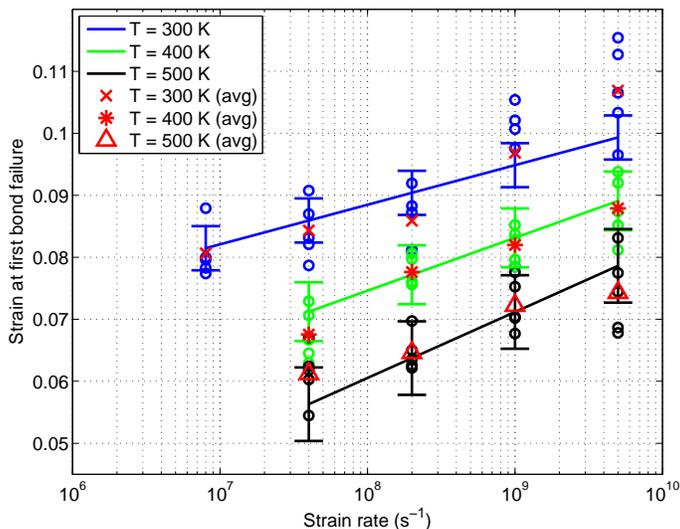
Figure 10: *Strain at first primary bond failure at several strain-rates and temperatures for a perfect 4×4×8 simulation cell using ReaxFF. The fitted colored lines represent the failure model predictions fitted to the data (open circles). Error bars are ±1 standard deviation as computed from the square root of variance in equation* (A.4). *Red markers represent average strain at first failure at the temperature indicated in the figure legend.*

slow strain rates failure is inevitable, but takes on average a very long time to occur.

4.4   Modeling hydrogen bond failure near isolated chain-end defects

Secondary hydrogen bonds between adjacent PPTA chains exhibit the same type of failure tendencies as primary bonds, as observed from the results in Section 3, and it is therefore reasonable to assert that analogous assumptions from reliability theory can be used to predict the onset of hydrogen bond failure. However, the mechanisms involved in hydrogen bond failure are different than those involved in covalent bond failure. For example, as mentioned in Section 3, hydrogen bonds will not fail in a perfect crystal of infinite-length chains subject to axial loading. Also, hydrogen bond failures cannot occur as isolated single bond failures, since for chain sliding to occur, multiple hydrogen bond failures must occur simultaneously between chains. For these reasons, some of the basic assumptions regarding primary bond failure, such as conceptualizing individual primary bonds as independently-operating
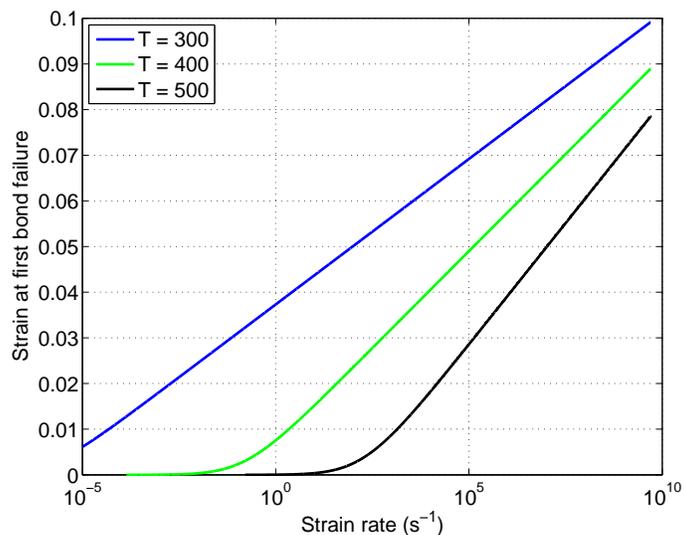
Figure 11: *Strain at first bond failure versus strain rate for temperatures of 300 K, 400 K, and 500 K as predicted by equation* (A.7)*.*

components with identical failure rates, do not apply to hydrogen bond failure.

Despite these complexities concerning the failure behavior of hydrogen bonds, it is possible to conceive of a chain-end defect distribution whereby the initiation of hydrogen bond failure at the chain-end defect sites can be treated in a very similar way as the failure of individual primary bonds in a perfect crystal. Consider a PPTA crystallite with a dilute concentration of chain-end defects. Suppose these defects are distributed throughout the crystal such that they can be accurately treated as non-interacting. That is, all the defects lie outside of each other's zone of influence, the region where both primary and secondary bonds alter their level of stretch in response to the presence of a nearby defect, as discussed in our previous work [8]. In this case, each chain-end defect site can be thought of as a component which behaves independently of other components in the system. Therefore, each defect site has an equal rate of failure, where failure is defined as the initiation of inter-chain slippage at the defect site. The initiation of inter-chain slippage is a somewhat complex event that involves the rupture of several hydrogen bonds near the defect. However, by treating defect sites as independently-operating components within the crystal, with a failure rate that depends on crystal strain and temperature, the initiation of chain slippage at these sites can be thought of as a failure event in the same way as the

Figure 12: *Chain-end defect distribution for MD simulations of hydrogen bond failure using the PCFF force field. Defects in adjacent chains are spaced 16 monomers apart along the z-axis of the crystallite.*

rupture of a covalent bond in the perfect crystal.

To explore this further, a system of isolated chain-end defects is constructed using a simulation cell of 3×8×64 unit cells, with each hydrogen-bonded sheet containing the chain-end distribution pattern depicted in Figure 12. The defects are uniformly spaced 16 monomers apart along the *z*-axis of the crystallite, and placed closer than this only when at least three chains separate the defects within a hydrogen bonded sheet. This ensures that each defect lies well outside of the zone of influence of all other defects in the crystal (about ±8 monomers along the broken chain axis relative to the defect, and ±4 monomers along the axes of adjacent chains [8]). The PCFF force field is then used to simulate the loading of this system at various strain-rate and temperature combinations. PCFF is used to study hydrogen bond rupture in the absence of primary bond rupture (primary bonds have essentially infinite strength in the PCFF force field). Despite the fact that ReaxFF would likely predict primary bond failure to be the favored mechanism in this system, conducting the study with PCFF is still a valid way to study the behavior of full-strength hydrogen bonds. To see chain sliding occur using ReaxFF, defect sites would need to be close enough to one another to weaken the hydrogen bonds near those sites, and any information gathered would be for hydrogen bonds in their weakened state, rather than at full strength. Chain slippage by hydrogen bond failure is assumed to occur when a hydrogen bond at the site exceeds an O–H distance of 5.5 Å. In strain-to-failure simulations of similar systems using PCFF, this distance criterion was visually estimated to be a good indicator that inter-chain slippage had initiated near a defect site.

To generate data on strain at first hydrogen bond failure for the defect pattern in Figure 12, a number of constant strain-rate loading simulations are conducted

at various rates and temperatures, and as with primary bonds in Section 4.3, a reliability modeling approach is taken where each chain-end defect site is treated as an independently-operating component with a time-dependent failure rate function $\lambda_0(\epsilon(t), T(t))$. The model is parameterized by fitting the strain at first failure data to the objective function defined in equation (14). The results are displayed in Figure 13, which, as for the case of primary bonds, show that a good fit to the data is obtained.

The best-fit parameters of the model to the data yield parameters $U_0 = 90.6$ kJ/mol, $\gamma = 414$ Å^3, and $\omega_0 = 2.2 \times 10^{11}$ Hz. Unlike the parameters extracted from examining primary bond failure data in Section 4.3, not all of these parameters lie in the expected range of values for hydrogen bonds. For example, the activation energy for hydrogen bonds has been experimentally observed to be in the range of 4–25 kJ/mol [62], which is significantly lower than the value of 90.6 kJ/mol obtained here. It is also expected that the activation energy for a hydrogen bond would be substantially lower than for a primary bond, which would be consistent with the activation energies cited in [62], yet it is just under 80% of the activation energy obtained for a primary bond (114 kJ/mol) in Section 4.3. Also, bond frequencies in the MD simulations conducted here are all on the order of 10^{13} Hz, so the value of ω_0 obtained here is lower than expected. However, care must be taken in interpreting the physical meaning of these parameters. The actual failure event in these simulations is the initiation of chain slippage near chain-end defect sites. The initiation of chain slippage requires the rupture of more than a single hydrogen bond, and as such, the activation energy parameter obtained here should actually be interpreted as the energy required to initiate chain-slippage, which requires multiple hydrogen bonds near the defect site to rupture. Similarly, the frequency parameter ω_0 does not represent the frequency of a single hydrogen bond, but rather some collective frequency measure of the group of bonds which fail, which may account for the lower-than-expected value obtained here. Considering these observations, the KTOF parameters obtained here for hydrogen bond rupture are reasonable, and as with the case of primary bonds, it can be concluded that the failure of hydrogen bonds near chain-end defects can be modeled via reliability theory, and that the assumption that failure rate can be determined by the proposed KTOF relation (4) is a good approximation to the actual bond behavior.
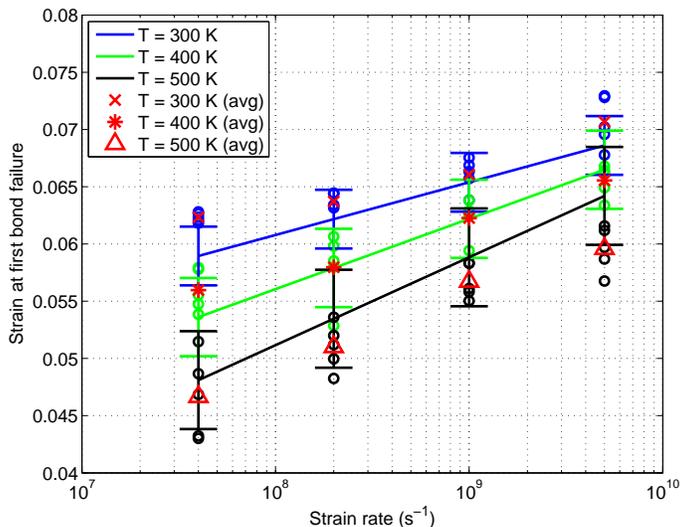
Figure 13: *Strain at first hydrogen bond failure at several strain-rates and temperatures for the pattern depicted in Figure 12, as simulated using PCFF. The fitted colored lines represent the failure model predictions fitted to the data (open circles). Error bars are ± 1 standard deviation as computed from the square root of variance in equation* (A.4). *Red markers represent average strain at first failure at the temperature indicated in the figure legend.*

4.5   Discussion

The results presented here demonstrate that it is possible to use concepts from reliability theory to predict the onset of both primary or secondary bond rupture in crystalline PPTA. The limitation of the model as presented is that predictions can only be made about the onset of first-bond failure, whether that is a primary bond (in the cases of a perfect crystallite or sufficiently sparse defect concentration) or secondary bond (in the case of clustered defects). To truly take advantage of this modeling approach to make predictions subsequent bond ruptures (and predict total crystallite failure) with arbitrary distributions of defects, a method must be developed to predict bond failure rates for bonds near pre-existing chain-end defects sites, as well as the change in bond failure rates after the first-bond rupture occurs in a crystallite. Our previous work [8] examined how bond stretch levels changed in bonds near chain-end defect sites, and this information could be used to characterize individual bond failure rates based on their location in the crystallite – bonds

experiencing increased stretch (stress concentration) will have higher rates of failure than bonds far away from defect sites, which will in turn have higher rates of failure than bonds experiencing decreased stretch (stress relaxation). Addressing how bond failure rates change after the first failed bond is more challenging. This is due to the conversion of bond potential energy into kinetic energy when a covalent bond rupture or chain-sliding event occurs. The diffusion of this kinetic energy into nearby PPTA chains creates a more severe disturbance of local crystal structure than does a pre-existing chain-end defect, therefore introducing stress concentrations in nearby bonds which are difficult to quantify due to the dynamic nature of the rupture event. If these items could be addressed, it would be possible to perform Monte-Carlo style simulations whereby crystalline PPTA is represented as a bead-spring array of bonds, each of which has individual failure probabilities computed based on their proximity to defects and the effects of recent nearby bond ruptures – a relatively simple version of such a model has been previously implemented by Termonia and Smith [63, 64] to make predictions about strain-rate effects in polymer fibers. Such a methodology would hypothetically allow the prediction of the strain-to-failure constitutive response of a crystallite with any defect distribution and under any loading conditions of interest.

5 Conclusion

This work has examined in detail the failure behavior of crystalline PPTA, particularly with respect to the influence of strain-rate and temperature in dynamic strain-to-failure simulations. The strain-to-failure simulation results in Section 3 show clear trends of increasing failure strain with increasing strain-rate and decreasing temperature, as well as dependence of failure strain on crystallite size, with larger crystallites exhibiting a lower failure strain compared to smaller crystallites under the same loading conditions. The dynamic strain-rate simulation results are particularly interesting when compared to the experimental observations of aramid fiber strain-rate sensitivity discussed in Section 1: the simulations conducted here show a clear strain-rate sensitivity of the crystallite strength, but not the modulus, suggesting that any experimentally observed modulus sensitivity may stem from fiber microstructure at a hierarchy above that of the individual crystallite (*e.g.*, inter-

crystallite interactions).

Through a variety of simulations, the crystallite failure behavior has been shown to be consistent with the kinetic theory of fracture, which postulates that failure in solids is driven by stress-assisted thermally fluctuating bonds whose likelihood of failure depends on temperature and loading conditions. In Section 4, a model was proposed which leverages concepts from reliability theory to make predictions about the onset of both primary and secondary bond failures, and was shown to yield physically realistic kinetic theory of fracture parameters when calibrated to MD simulation results. In addition to offering further confirmation that PPTA crystallite failure is well-characterized by the kinetic theory of fracture, the model represents a promising starting point for deducing an approach to predicting the onset of crystallite failure (rather than first-bond failure as done here) based on bond fluctuation statistics, rather than relying on costly MD simulations. In particular, such an approach would allow the prediction of failure in crystallites too large and/or at strain-rates too slow to be feasibly simulated using MD.

The combined contribution of this work and our previous work [8], which addressed the important role that chain-end defects play in both the strength and modulus of a crystallite, is an improved understanding of the PPTA polymer chain mechanics and PPTA crystallite mechanical behavior. These findings could serve as a foundation for developing a constitutive model for a single PPTA crystallite containing defects, which in turn is a good basis for developing a multiscale model for predicting the behavior of single aramid fibers. There is significant value in adopting a multiscale modeling approach for aramid fibers due to their microstructural complexities. Indeed, a multiscale aramid fiber model could account for specific defect patterns, chain lengths, or other known microstructural characteristics in order to make predictions about a fiber's constitutive behavior, thus leading to a continuum-scale constitutive model based on specific knowledge of a fiber's microstructure.

References

1. Northolt, M. X-ray diffraction study of poly(p-phenylene terephthalamide) fibres. *European Polymer Journal* **10,** 799–804 (1974).

2. Dobb, M., Johnson, D. & Saville, B. Direct observation of structure in high-modulus aromatic fibers. *Journal of Polymer Science: Polymer Symposia* **58,** 237–251 (1977).

3. Dobb, M., Johnson, D. & Saville, B. Supramolecular structure of a high-modulus polyaromatic fiber (Kevlar 49). *Journal of Polymer Science: Polymer Physics Edition* **15,** 2201–2211 (1977).

4. Dobb, M., Johnson, D. & Saville, B. Structural aspects of high modulus polyamide fibres. *Philosophical Transactions of the Royal Society of London. Series A, Mathemetical and Physical Sciences* **294,** 483–485 (2013).

5. Panar, M., Avakian, P., Blume, R., Gardner, K., Gierke, T. & Yang, H. Morphology of Poly (p-Phenylene Terephthalamide) fibers. *Journal of Polymer Science: Polymer Physics Edition* **21,** 1955–1969 (1983).

6. Morgan, R., Pruneda, C. & Steele, W. The relationship between the physical structure and the microscopic deformation and failure processes of Poly(p-Phenylene Terephthalamide) fibers. *Journal of Polymer Science: Polymer Physics Edition* **21,** 1757–1783 (1983).

7. Li, L., Allard, L. & Bigelow, W. On the morphology of aromatic polyamide fibers (Kevlar, Kevlar-49, and PRD-49). *Journal of Macromolecular Science, Part B* **22,** 269–290 (1983).

8. Mercer, B., Zywicz, E. & Papadopoulos, P. Molecular dynamics modeling of PPTA crystallite mechanical properties in the presence of defects. *Polymer* **114,** 329–347 (2017).

9. Wang, Y. & Xia, Y. The effects of strain rate on the mechanical behaviour of kevlar fibre bundles: an experimental and theoretical study. *Composites Part A: Applied Science and Manufacturing* **29,** 1411–1415 (1998).

10. Tan, V., Zeng, X. & Shim, V. Characterization and constitutive modeling of aramid fibers at high strain rates. *International Journal of Impact Engineering* **35,** 1303–1313 (2008).

11. Gu, B. Analytical modeling for the ballistic perforation of planar plain-woven fabric target by projectile. *Composites Part B* **34,** 361–371 (2003).

12. Languerand, D., Zhang, H., Murthy, N., Ramesh, K. & Sansoz, F. Inelastic behavior and fracture of high modulus polymeric fiber bundles at high strain-rates. *Materials Science and Engineering A* **500,** 216–224 (2009).

13. Lim, J., Zheng, J. Q., Masters, K. & Chen, W. W. Effects of gage length, loading rates, and damage on the strength of PPTA fibers. *International Journal of Impact Engineering* **38,** 219–227 (2011).

14. Cheng, M., Chen, W. & Weerasooriya, T. Mechanical properties of Kevlar® KM2 single fiber. *Journal of Engineering Materials and Technology* **127,** 197–203 (2005).

15. Shim, V., Lim, C. & Foo, K. Dynamic mechanical properties of fabric armour. *International Journal of Impact Engineering* **25,** 1–15 (2001).

16. van Duin, A., Dasgupta, S., Lorant, F. & Goddard III, W. ReaxFF: A reactive force field for hydrocarbons. *The Journal of Physical Chemistry A* **105,** 9396–9409 (2001).

17. van Duin, A., Strachan, A., Stewman, S., Zhang, Q., Xu, X. & Goddard III, W. ReaxFF SiO reactive force field for Silicon and Silicon Oxide systems. *Journal of Physical Chemistry A* **107,** 3803–3811 (2003).

18. Shin, Y., Kwak, H., Zou, C., Vasenkov, A. & van Duin, A. Development and validation of a ReaxFF reactive force field for Fe/Al/Ni alloys: Molecular dynamics study of elastic constants, diffusion, and segregation. *The Journal of Physical Chemistry A* **116,** 12163–12174 (2012).

19. Nielson, K., van Duin, A., Oxgaard, J., Deng, W.-Q. & Goddard III, W. Development of the ReaxFF reactive force field for describing transition metal catalyzed reactions, with application to the initial stages of the catalytic formation of carbon nanotubes. *Journal of Physical Chemistry A* **109,** 493–499 (2005).

20. Sun, H., Mumby, S., Maple, J. & Hagler, A. An ab initio CFF93 all-atom force field for polycarbonates. *Journal of the American Chemical Society* **116,** 2978–2987 (1994).

21. Tobolsky, A. & Eyring, H. Mechanical properties of polymeric materials. *The Journal of Chemical Physics* **11,** 125 (1943).

22. Zhurkov, S. Kinetic concept of the strength of solids. *International Journal of Fracture* **1,** 311–323 (1965).

23. Zhurkov, S. & Korsukov, V. Atomic mechanism of fracture of solid polymers. *Journal of Polymer Science: Polymer Physics Edition* **12,** 385–398 (1974).

24. Jensen, B., Wise, K. & Odegard, G. The effect of time step, thermostat, and strain rate on ReaxFF simulations of mechanical failure in diamond, graphene, and carbon nanotube. *Journal of Computational Chemistry* **36,** 1587–1596 (2015).

25. Sen, D., Novoselov, K., Reis, P. & Buehler, M. Tearing graphene sheets from adhesive substrates produces tapered nanoribbons. *Small* **6,** 1108–1116 (2010).

26. Kim, K., Artyukhov, V., Regan, W., Liu, Y., Crommie, M., Yakobson, B. & Zettl, A. Ripping graphene: Preferred directions. *Nano Letters* **12,** 293–297 (2012).

27. Cranford, S. & Buehler, M. Mechanical properties of graphyne. *Carbon* **49,** 4111–4121 (2011).

28. Cranford, S., Brommer, D. & Buehler, M. Extended graphynes: simple scaling laws for stiffness, strength and fracture. *Nanoscale* **4,** 7797–7809 (2012).

29. Buehler, M., van Duin, A. & Goddard III, W. Multiparadigm modeling of dynamical crack propagation in Silicon using a reactive force field. *Physical Review Letters* **96,** 095505 (2006).

30. Yilmaz, D. Modeling failure mechanisms of poly (p-phenylene terephthalamide) fiber using reactive potentials. *Computational Materials Science* **109,** 183–193 (2015).

31. Chowdhury, S. C., Sockalingam, S. & Gillespie Jr., J. W. Molecular dynamics modeling of the effect of axial and transverse compression on the residual tensile properties of ballistic fiber. *Fibers* **5,** 1–16 (2017).

32. Liu, L., Liu, Y., Zybin, S., Sun, H. & Goddard III, W. ReaxFF-lg: Correction of the ReaxFF reactive force field for London dispersion, with applications to the equations of state for energetic materials. *The Journal of Physical Chemistry A* **115,** 11016–11022 (2011).

33. Rutledge, G. & Suter, U. Detailed atomistic simulation of oriented pseudocrystalline polymers and application to a stiff-chain aramid. *Macromolecules* **24,** 1921–1933 (1991).

34. Rutledge, G. & Suter, U. Calculation of mechanical properties of poly(p-phenylene terephthalamide) by atomistic modelling. *Polymer* **32,** 2179–2189 (1991).

35. Lacks, D. & Rutledge, G. Thermal Expansion and Temperature Dependence of Elastic Moduli of Aromatic Polyamides. *Macromolecules* **27,** 7197–7204 (1994).

36. Lacks, D. Molecular simulation of compressive failure in poly(p-phenylene teraphthalamide) crystals. *Journal of Materials Science* **31,** 5885–5889 (1996).

37. Sun, H. COMPASS: An ab initio force-field optimized for condensed-phase applications – Overview with details on Alkane and Benzene compounds. *Journal of Physical Chemistry B* **102,** 7338–7364 (1998).

38. Grujicic, M., Bell, W., Glomski, P., Pandurangan, B., Yen, C.-F. & Cheeseman, B. Filament-level modeling of aramid-based high-performance structural materials. *Journal of Materials Engineering and Performance* **20,** 1401–1413 (2011).

39. Grujicic, M., Glomski, P., Pandurangan, B., Bell, W., Yen, C.-F. & Cheeseman, B. Multi-length scale computational derivation of Kevlar® yarn-level material model. *Journal of Materials Science* **46,** 4787–4802 (2011).

40. Grujicic, M., Pandurangan, B., Snipes, J., Yen, C.-F. & Cheeseman, B. Multi-length scale-enriched continuum-level material model for Kevlar®-fiber-reinforced polymer-matrix composites. *Journal of Materials Engineering and Performance* **22,** 681–695 (2013).

41. Grujicic, M., Yavari, R., Ramaswami, S., Snipes, J., Yen, C.-F. & Cheeseman, B. Molecular-level study of the effect of prior axial compression/torsion on the axial-tensile strength of PPTA fibers. *Journal of Materials Engineering and Performance* **22,** 3269–3287 (2013).

42. Grujicic, M., Ramaswami, S., Snipes, J., Yavari, R., Yen, C.-F. & Cheeseman, B. Formation and propagation of Single p-Phenylene terephthalamide (PPTA) fibers. *Advances in Materials Science and Engineering* **2013,** 1–15 (2013).

43. Grujicic, M., Yavari, R., Snipes, J., Ramaswami, S., Yen, C.-F. & Cheeseman, B. The effect of plain-weaving on the mechanical properties of warp and weft p-phenylene terephthalamide (PPTA) fibers/yarns. *Journal of Materials Science* **49,** 8272–8293 (2014).

44. Plimpton, S. Fast parallel algorithms for short-range molecular dynamics. *Journal of Computational Physics* **117,** 1–19 (1995).

45. Accelrys Software Inc. *Materials Studio* San Diego, 2011.

46. Nosé, S. A unified formulation of the constant temperature molecular dynamics methods. *The Journal of Chemical Physics* **81,** 511–519 (1984).

47. Hoover, W. Canonical dynamics: Equilibrium phase-space distributions. *Physical Review A* **31,** 1695–1697 (1985).

48. Martyna, G. J., Tobias, D. J. & Klein, M. L. Constant pressure molecular dynamics algorithms. *The Journal of Chemical Physics* **101,** 4177–4189 (1994).

49. Hossain, D., Tschopp, M., Ward, D., Bouvard, J., Wang, P. & Horstemeyer, M. Molecular dynamics simulations of deformation mechanisms of amorphous polyethylene. *Polymer* **51,** 6071–6083 (2010).

50. Rappé, A. & Goddard III, W. Charge equilibration for molecular dynamics simulations. *The Journal of Physical Chemistry* **95,** 3358–3363 (1991).

51. Nakano, A. Parallel multilevel preconditioned conjugate-gradient approach to variable-charge molecular dynamics. *Computer Physics Communications* **104,** 59–69 (1997).

52. Aktulga, H., Pandit, S., van Duin, A. & Grama, A. Reactive molecular dynamics: Numerical methods and algorithmic techniques. *SIAM Journal on Scientific Computing* **34,** C1–C23 (2012).

53. Hockney, R. & Eastwood, J. *Computer Simulation Using Particles* (Taylor & Francis Group, New York, NY, 1988).

54. Tsai, D. H. The virial theorem and stress calculation in molecular dynamics. *The Journal of Chemical Physics* **70,** 1375 (1979).

55. Gu, B. Ballistic penetration of conically cylindrical steel projectile into plain-woven fabric target - A finite element simulation. *Journal of Composite Materials* **38,** 2049–2074 (2004).

56. O'Connor, T. C. & Robbins, M. O. Chain ends and the ultimate strength of Polyethylene fibers. *ACS Macro Letters* **5,** 263–267 (2016).

57. Hsiao, C. C. Fracture. *Physics Today* **19,** 49–53 (1966).

58. Høyland, A. & Rausand, M. *System Reliability Theory: Models, Statistical Methods, and Applications* 2nd, 15–63 (John Wiley & Sons, Inc., Hoboken, New Jersey, 1994).

59. Hansen, A. & Baker-Jarvis, J. A rate dependent kinetic theory of fracture for polymers. *International Journal of Fracture* **44,** 221–231 (1990).

60. Roylance, D. Some consequences of a fracture criterion for oriented polymers based on electron spin resonance spectoscopy. *International Journal of Fracture* **21,** 107–114 (1981).

61. Byrd, R. H., Nocedal, J. & Waltz, R. A. in *Large-Scale Nonlinear Optimization* (eds di Pillo, G. & Roma, M.) 35–59 (Springer-Verlag, 2006).

62. Sheu, S.-Y., Yang, D.-Y., Selzle, H. & Schlag, E. Energetics of hydrogen bonds in peptides. *Proceedings of the National Academy of Sciences of the United States of America* **100,** 12683–12687 (2003).

63. Termonia, Y. & Smith, P. Theoretical study of the ultimate mechanical properties of poly(p-phenylene- terephthalamide) fibres. *Polymer* **27,** 1845–1849 (1986).

64. Termonia, Y. & Smith, P. *A theoretical approach to the calculation of the maximum tensile strength of polymer fibers* (eds Zachariades, A. & Porter, R. S.) 321–362 (Marcel Dekker, Inc., New York, NY, 1988).

65. Gautschi, W. & Cahill, W. F. in *Handbook of Mathematical Functions with Formulas, Graphs, and Mathematical Tables* (eds Milton, A. & Stegun, I.) 10th. Chap. 5 (Dover, New York, 1972).

Appendix

A Summary of pertinent reliability theory principles and equations

Let the time-to-failure τ of a component or system be a continuous random variable in time with continuous probability density function (PDF) $f(t)$. In reliability theory, system failure is more commonly discussed in terms of the hazard rate (or failure rate) $h(t)$, which represents the instantaneous rate of failure conditional on failure having not occurred before time t. The PDF of the system is related to $h(t)$ by

$$f(t) = h(t) \exp\left[-\int_0^t h(t')\,dt'\right] \ . \tag{A.1}$$

One may compute the probability that the component of interest survives until time t (or, equivalently, that failure occurs after time t), which is given by the survival function $S(t) = \int_t^\infty f(t')\,dt'$. The relationship between $S(t)$ and $h(t)$ is therefore

$$S(t) \;=\; \exp\left[-\int_0^t h(t')\,dt'\right] \ . \tag{A.2}$$

The mean time-to-failure t_f equals the expectation $\mathrm{E}(\tau)$, which can be shown to be

$$t_f \;=\; \int_0^\infty S(t)\,dt \ . \tag{A.3}$$

Similarly, the variance σ^2 of the mean time-to-failure may be expressed as

$$\sigma^2 \;=\; \int_0^\infty 2tS(t)\,dt - t_f^2 \ . \tag{A.4}$$

A system may comprise a collection of components, each with its own failure rate. A *series* system is a configuration in which failure of a single component results in system failure. The failure rate h_{sys} of a series system of components which operate independently of one another is the algebraic sum of the individual failure rates of the components, that is,

$$h_{sys} \;=\; \sum_{i=1}^N h_i \ , \tag{A.5}$$

where h_i, $i = 1, 2, \ldots, N$, is the failure rate of component i in a system with N components.

B Reliability theory prediction of first-bond failure strain under strain-rate crystallite loading

Starting from the failure rate function defined in equation (12), the failure rate function for a system of N bonds is $\hat{\lambda}_N(t, \dot{\epsilon}, T) = N\hat{\lambda}_0(t, \dot{\epsilon}, T)$, and applying equation (A.2), the survival function for the system takes the form

$$
\begin{aligned}
S(t, \dot{\epsilon}, T) &= \exp\left[-\int_0^t \hat{\lambda}_N(t', \dot{\epsilon}, T)\, dt'\right] \\
&= \exp\left[\frac{\omega_0 N k_b T}{\gamma E \dot{\epsilon}}\left(1 - \exp\left[\frac{\gamma E \dot{\epsilon} t}{k_b T}\right]\right)\right] .
\end{aligned}
\tag{A.6}
$$

With the survival function defined, the mean time-to-first-bond failure under constant strain-rate loading may be calculated according to equation (A.3) and the failure strain at first-bond failure ϵ_{fb} is then found to be equal to

$$
\epsilon_{fb} = \dot{\epsilon} t_{f_N} = -\frac{k_b T}{\gamma E} \exp(C)\, \mathrm{Ei}(-C) ,
\tag{A.7}
$$

where the constant C is given by

$$
C = \frac{\omega_0 N k_b T}{\gamma E \dot{\epsilon}} \exp\left(-\frac{U_0}{k_b T}\right) ,
\tag{A.8}
$$

and $\mathrm{Ei}(x)$ is the exponential integral function. Using series expansions for the exponential and exponential integral terms [65], ϵ_{fb} can be expressed as

$$
\epsilon_{fb} \doteq \frac{k_b T}{\gamma E}\left(-\ln(C) - G + O(C)\right) ,
\tag{A.9}
$$

where G is the Euler-Mascheroni constant. When C is small, e.g. for large strain rates, the $O(C)$ term in equation (A.9) becomes negligible, and the expected strain at first-bond failure can be approximated as

$$
\epsilon_{fb} \approx \frac{k_b T}{\gamma E}\left(-\ln(C) - G\right) .
\tag{A.10}
$$